# NoiseShift: Resolution-Aware Noise Recalibration for Better Low-Resolution Image Generation

Ruozhen He Moayed Haji-Ali Ziyan Yang Vicente Ordonez Rice University

{catherine.he, mh155, zy47, vicenteor}@rice.edu

### **Abstract**

Text-to-image diffusion models trained on a fixed set of resolutions often fail to generalize, even when asked to generate images at lower resolutions than those seen during training. High-resolution text-to-image generators are currently unable to easily offer an out-of-the-box budget-efficient alternative to their users who might not need high-resolution images. We identify a key technical insight in diffusion models that when addressed can help tackle this limitation: Noise schedulers have unequal perceptual effects across resolutions. The same level of noise removes disproportionately more signal from lower-resolution images than from highresolution images, leading to a train-test mismatch. We propose NoiseShift, a training-free method that recalibrates the noise level of the denoiser conditioned on resolution size. NoiseShift requires no changes to model architecture or sampling schedule and is compatible with existing models. When applied to Stable Diffusion 3, Stable Diffusion 3.5, and Flux-Dev, quality at low resolutions is significantly improved. On LAION-COCO, NoiseShift improves SD3.5 by 15.89%, SD3 by 8.56%, and Flux-Dev by 2.44% in FID on average. On CelebA, NoiseShift improves SD3.5 by 10.36%, SD3 by 5.19%, and Flux-Dev by 3.02% in FID on average. These results demonstrate the effectiveness of NoiseShift in mitigating resolution-dependent artifacts and enhancing the quality of low-resolution image generation.

#### 1. Introduction

Diffusion models [28, 29, 32] have emerged as a powerful class of generative models, achieving state-of-the-art performance in generating high-fidelity images [36–38]. However, they struggle to generalize to resolutions other than those seen during the final training stages. Despite being architecturally capable of handling multiple resolutions, these models struggle at lower resolutions, producing low-fidelity images with artifacts and incoherent content [12]. Generating images at lower resolutions reduces computational cost,

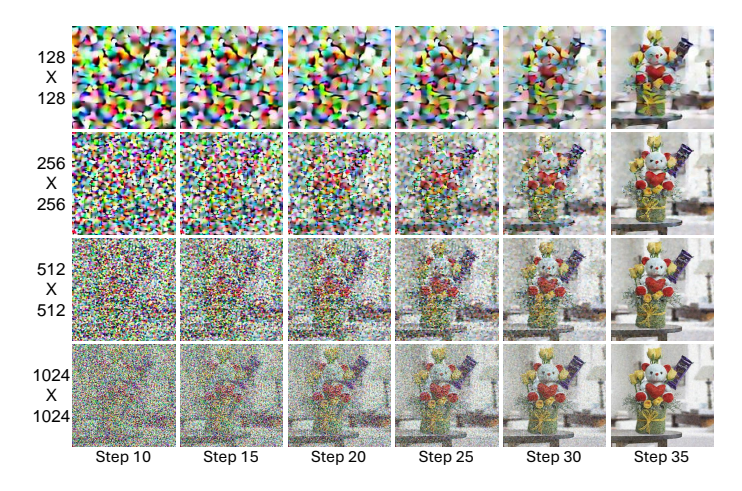
making it preferable for real-world scenarios that demand fast, lightweight generation—such as mobile deployment, rapid prototyping, and large-scale sampling.

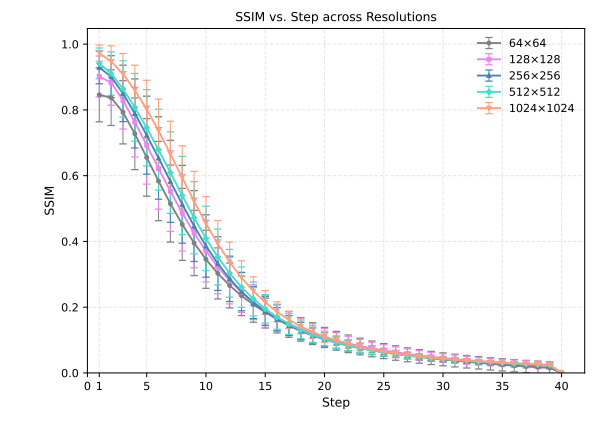
Low-resolution generation is not just a fallback for limited compute environments, but it is foundational to efficiency and scalability. Diffusion models require iterative denoising over hundreds of steps, and the cost grows quadratically with resolution. A common training recipe to train such models involves progressively increasing resolution, starting with low-resolution inputs and fine-tuning on higher-resolution data. Despite being pre-trained on lower-resolution data, models fine-tuned at high resolution often lose their ability to generate high-quality low-resolution images. Recent studies show that diffusion models degrade significantly when sampling at resolutions outside the final fine-tuning set—even when those low resolutions appeared earlier in training [7, 12, 40]. These failures are often attributed to architectural limitations in generalizing across spatial scales [28, 33].

Previous attempts aim to improve resolution generalization by fine-tuning lightweight adapters for each specified resolution [5, 30]. However, such methods are computationally expensive and impractical for current large scale state-of-the-art text-to-image models [6, 9]. Other research proposed training-free ad-hoc and aim to constrain the model prediction at resolutions from the post-training set [2, 12, 17, 31, 39, 40], or generate the images in multiple stages [7]. However, these solutions often increase inference cost and focus mostly on high-resolution synthesis.

A more subtle but critical issue is *exposure bias*—the discrepancy between training-time noise distributions and those seen during inference [18, 21, 41]. Recent work mitigates this by altering the inference noise schedule [21]. These fixes apply across resolutions, but they do not fully resolve the underlying perceptual mismatch.

In this paper, we show that the exposure bias is magnified at lower resolutions. Although the signal-to-noise ratio (SNR) is nominally fixed across resolutions for all diffusion timesteps, the same absolute noise power erases a larger fraction of perceptual signal in a low-resolution image than in a high-resolution variant [16]. It has been shown that low-





(a) Visual comparison of forward noise at fixed  $\sigma_t$  across resolutions at timesteps t=10,15,20,25,30,35. The same noise level leads to perceptually stronger corruption at lower resolutions.

(b) SSIM between clean image  $\mathbf{x}_0$  and forward-noised image  $\mathbf{x}_t$  at different resolutions. The same  $\sigma_t$  induces lower SSIM at lower resolutions.

Figure 1. Resolution-dependent perceptual effect of noise. At the same sampling noise level  $\sigma_t$ , lower-resolution images experience more severe visual and structural corruption than high-resolution counterparts.

resolution images lose semantic details more rapidly due to pixel aggregation, while high-resolution images retain details due to spatial redundancy [16] (see Figure 1) Consequently, for any given timestep t, a model must denoise images drawn from a distribution increasingly distant from the one it was trained on, leading to a pronounced loss in fidelity. The time-shifting sampling schedule can provide a remedy to reduce the exposure bias for each resolution [6], but the timestep value passed as a conditioning input remains unchanged. Therefore, the model still gets a noise distribution that it never saw during training, leaving a residual train-test mismatch. This limitation motivates our resolution-aware method that goes beyond scheduler adjustments alone.

We propose NoiseShift, a simple, training-free test-time calibration method that aligns the reverse diffusion process with a resolution-dependent distribution. The key to our method is to control the noise level conditioning of the pretrained diffusion model to align the predictions across resolutions. NoiseShift adjusts the noise-level condition to better reflect the perceptual noise in the image based on its resolution, thereby reducing exposure bias when generating lower-resolution images.

Specifically, we perform a coarse-to-fine grid search to learn a resolution-specific mapping of the conditioning value that minimizes the denoising error prediction, effectively substituting the nominal timestep t with a surrogate timestep  $\tilde{t}$  whose noise distribution matches those seen during training. At inference, we preserve the standard schedule but feed the network this calibrated timestep conditioning, aligning the reverse process with the true noise distribution, mitigating exposure bias, and improving overall quality. NoiseShift

is lightweight, simple, training-free, and provides consistent improvements. When applied to SD3.5 [9], NoiseShift improves FID by an average of 15.89% on LAION-COCO and 10.36% on CelebA. We further validate NoiseShift on Flux [6] and obtain consistent improvements of an average 2.44% FID on LAION-COCO and 3.02% FID on CelebA.

### 2. Related Work

Diffusion Models at Arbitrary Resolutions. Most diffusion models are trained at a single, fixed size, but real applications demand flexible outputs. Multiple works have been proposed to adapt pretrained diffusion models to variable resolutions in a training or training-free manner [5, 7, 10, 31, 39, 40]. Multidiffusion [2] stitches multiple overlapping diffusion windows, enabling panoramas and extreme aspect ratios without retraining. ElasticDiffusion [12] separates global structure and local detail during decoding, allowing a pretrained model to scale up or down in resolution while remaining artifact-free. ScaleCrafter [13] enlarges the pretrained diffusion model receptive field onthe-fly via re-dilation and couples it with noise-damped guidance, achieving 4K resolution from a 512p model. These methods highlight that inference-time adaptations can unlock arbitrary-size synthesis, yet none address the noise-level misalignment that emerges when the same schedule is reused across resolutions.

**Test-Time Calibration and Denoising Consistency.** A complementary direction of research focuses on inference-time strategies to calibrate the diffusion process and improve the generation quality. Chen *et al.* [4] show that

default linear or cosine schedules leave a residual signal and propose schedule rescaling to close this train—test gap. WSNR Sampling [11] refines the schedule to keep a constant weighted SNR across domains, boosting high-res fidelity. ScaleCrafter [13] further introduces noise-dependent classifier-free guidance, lowering guidance in early noisy steps and increasing it later. Time-shifting [21] adjusts the sampling scheduler during inference to reduce exposure bias. High-order ODE solvers such as the DPM-Solver [25, 26] shorten the sampling trajectory while preserving consistency. Our work is complementary, instead of modifying the global schedule or the sampler, we re-index the timestep embedding to *fool* the model into operating at the correct noise level for each resolution.

Perceptual Effects of Noise Across Resolutions. Resolution changes alter how noise corrupts perceptual content. Jin *et al.* [19] observe that when prompting a pretrained diffusion model to generate images outside their training set, low-res images lose fine details, whereas high-res outputs duplicate objects, and proposed an entropy-based attention scale to mitigate this issue. ScaleCrafter [13] and ElasticD-iffusion [12] report similar artifacts and attribute them to a limited receptive field. Chen *et al.* [3] quantify that a fixed noise percentage degrades  $256 \times 256$  images far more than  $1024 \times 1024$  images, motivating scale-aware schedules, which several subsequent work formalized [11, 21]. These studies underline that identical timesteps correspond to *different* perceptual noise levels across resolutions, a mismatch NoiseShift explicitly corrects.

### 3. Method

This section presents our resolution-aware test-time calibration approach for flow-matching diffusion models. We aim to optimize the forward–reverse misalignment observed when sampling at resolutions different from the training resolution. We begin by reviewing the flow matching framework (Sec. 3.1). We then analyze how resolution affects forward-reverse consistency (Sec. 3.2), and introduce NoiseShift, our training-free method to calibrate the conditioning noise level through coarse-to-fine grid search (Sec. 3.3). This calibration is performed once per resolution and reused during inference without modifying the model or the noise schedule.

### 3.1. Preliminaries: Flow Matching

Flow matching [22, 23] is a training paradigm for generative models that learns a continuous transformation from a simple base distribution  $p_0(\mathbf{x})$  (e.g., Gaussian noise) to a complex target distribution  $q(\mathbf{x})$ . It directly regresses the velocity field of an ordinary differential equation (ODE), enabling simulation-free learning of the generative process. The trajectory is defined as a continuous interpolation be-

tween a noisy sample  $\mathbf{x}_0 \sim p_0$  and a data point  $\mathbf{x}_1 \sim q$  along a predefined path.

The training objective minimizes the discrepancy between a predicted velocity  $v_t(\mathbf{x}_t)$  and a target velocity  $u_t(\mathbf{x}_t \mid \mathbf{x}_1)$ , which is analytically derived from the interpolation path:

$$\mathbb{E}_{t,\mathbf{x}_1,\mathbf{x}_t \sim p_t(\cdot \mid \mathbf{x}_1)} \left[ \|v_t(\mathbf{x}_t) - u_t(\mathbf{x}_t \mid \mathbf{x}_1)\|^2 \right], \quad (1)$$

where  $\mathbf{x}_t$  follows a time-dependent interpolant between  $\mathbf{x}_0$  and  $\mathbf{x}_1$ , such as:

$$\mathbf{x}_t = t \, \mathbf{x}_1 + (1 - t) \, \mathbf{x}_0, \quad \mathbf{x}_t \sim \mathcal{N}(t \, \mathbf{x}_1, (1 - t)^2 \mathbf{I}).$$
 (2)

This framework has been adopted in recent diffusion transformers such as Stable Diffusion 3 [1] and Flux [6], which we study in this paper. These models generate images by integrating the learned velocity field over a predefined noise schedule  $\{\sigma_t\}$ , where our method intervenes at test time to correct resolution-specific inconsistencies.

### 3.2. Train-Test Misalignment in Diffusion Sampling

While flow-matching diffusion models are trained to simulate noise removal, the reverse denoising process at test time can deviate from the original forward trajectory. This discrepancy introduces a hidden source of error, particularly at resolutions different from those used during training.

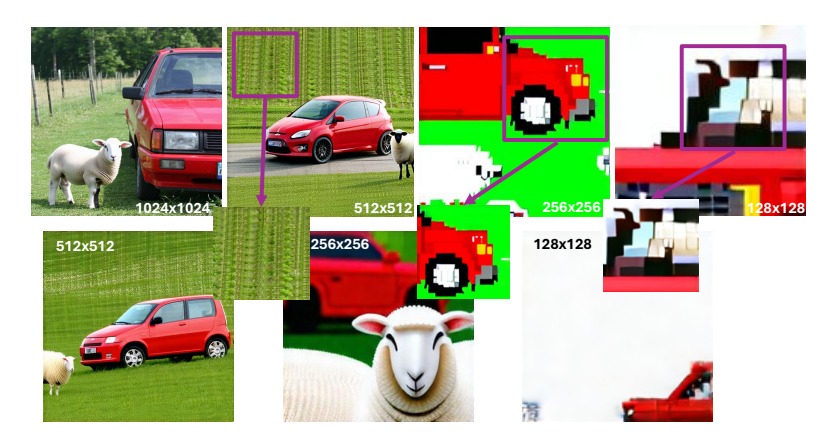
Forward–Reverse Inconsistency at Test Time. In principle, a diffusion model trained via flow matching learns to reverse the forward noise process. However, we observe a systematic discrepancy between the noisy sample  $\mathbf{x}_t$  obtained by adding noise to a clean image  $\mathbf{x}_0$ , and the prediction  $\hat{\mathbf{x}}_t$  produced by a single-step denoising operation:

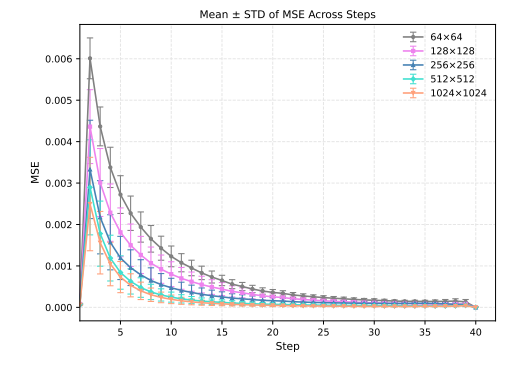
$$\hat{\mathbf{x}}_t = \text{EulerStep}(\mathbf{x}, \sigma_t) \not\approx \mathbf{x}_t = \text{AddNoise}(\mathbf{x}_0, \sigma_t).$$
 (3)

Even when the same sampling noise level  $\sigma_t$  is used, the denoised prediction does not align with the expected noisy image, revealing a time inconsistency in the learned velocity field.

To evaluate this effect, we progressively add noise to a clean image to obtain a trajectory  $\mathbf{x}_0, \mathbf{x}_1, \dots, \mathbf{x}_T$ . At a selected timestep t, we apply a single reverse Euler step to  $\mathbf{x}_t$  to obtain  $\hat{\mathbf{x}}_{t-1}$ , then compare it to the ground-truth forward image  $\mathbf{x}_{t-1}$ . We perform it on a set of random images and compute the mean squared error (MSE) between  $\hat{\mathbf{x}}_{t-1}$  and  $\mathbf{x}_{t-1}$ .

As shown in Figure 2, this discrepancy exists even at the training resolution and becomes more severe as image resolution diverges. Panel (a) illustrates the conceptual gap between forward and reverse operations, while panel (b) shows that the MSE grows sharply at early steps and at lower resolutions. These findings suggest that the model's denoising behavior is not intrinsically aligned with the resolution-invariant assumptions of the noise schedule.





(a) Visual degradation at unfamiliar resolutions. Besides cropping artifacts likely caused by positional encodings, generated images often exhibit structural glitches and texture breakdowns (top). Our method (bottom) improves visual fidelity by calibrating the conditioning noise level without retraining or architectural changes.

(b) MSE between forward and reverse trajectories across timesteps t at different resolutions. Misalignment increases with resolution shift, especially at early steps.

Figure 2. Training-testing misalignment in diffusion sampling. The forward (noise addition) and reverse (denoising) processes are theoretically symmetric but diverge during test-time sampling. (a) illustrates the conceptual discrepancy. (b) plots the mean squared error between the predicted and actual noisy image across sampling steps.

**Resolution-Dependent Misalignment.** While minor forward-reverse discrepancies are expected due to training limitations and imperfect regression of the velocity field, we observe that these inconsistencies vary systematically with resolution. In particular, the misalignment becomes substantially worse when sampling at resolutions that deviate from the model's training resolution.

To understand this phenomenon, we compare the outputs of the forward noise process across different resolutions using the same noise level  $\sigma_t$ . As shown in Figure 1(a), more signal is destroyed in the low-resolution images in this forward process compared to the high-resolution ones, despite the shared diffusion schedule  $\{\sigma_t\}$ . This suggests that the perceptual impact of noise is resolution-dependent.

We hypothesize that this effect arises from spatial compression. In low-resolution images, each pixel encodes a larger region of semantic content, so adding noise disproportionately disrupts meaningful structure. In contrast, highresolution images have greater spatial redundancy, which makes the same level of noise less perceptually destructive. As a result, a fixed  $\sigma_t$  induces qualitatively different levels of corruption depending on resolution.

To quantify this, we analyze SSIM between clean images  $\mathbf{x}_0$  and their forward-noised counterparts  $\mathbf{x}_t$  across multiple resolutions. Figure 1(b) shows that SSIM consistently degrades more rapidly at lower resolutions. These trends mirror the MSE-based forward-reverse misalignment described in Figure 2, further reinforcing the link between perceptual degradation and resolution.

Together, these findings reveal a fundamental samplingtime issue: diffusion models assume resolution-invariant

## Algorithm 1 Coarse-to-Fine Conditioning Noise Calibration **Require:** Model $\phi$ , clean image $\mathbf{x}_0$ , noise schedule $\{\sigma_t\}$ ,

```
timestep t, upper bound \hat{\sigma}_{t+1}^*
1: \mathbf{x}_{t+1} \leftarrow \text{AddNoise}(\mathbf{x}_0, \sigma_{t+1})
2: \mathbf{x}_t \leftarrow \text{AddNoise}(\mathbf{x}_0, \sigma_t)
3: Initialize \hat{\sigma}_t^* \leftarrow \sigma_t, \mathcal{L}^* \leftarrow \|\hat{\mathbf{x}}_t - \mathbf{x}_t\|^2
4: Set coarse search range: \tilde{\sigma} \in [\max(0, \sigma_t - 1)]
     (\epsilon_c), \min(\hat{\sigma}_{t+1}^*, \sigma_t + \epsilon_c)]
5: for all \tilde{\sigma} \in coarse candidates (stride \delta_c) do
```

- $\hat{\mathbf{x}}_t \leftarrow \mathbf{x}_{t+1} + \phi(\mathbf{x}_{t+1}, \tilde{\sigma}) \cdot \Delta t$
- $\mathcal{L} \leftarrow \|\hat{\mathbf{x}}_t \mathbf{x}_t\|^2$ 7:
- if  $\mathcal{L} < \mathcal{L}^*$  then
- $\hat{\sigma}_t^* \leftarrow \tilde{\sigma}, \quad \mathcal{L}^* \leftarrow \mathcal{L}$ 9:
- end if 10.
- 11: end for
- 12: Set fine search range:  $\tilde{\sigma} \in [\max(0, \hat{\sigma}_t^* (\epsilon_f), \min(\hat{\sigma}_{t+1}^*, \hat{\sigma}_t^* + \epsilon_f)]$
- 13: **for all**  $\tilde{\sigma} \in$  fine candidates (stride  $\delta_f$ ,  $\delta_f < \delta_c$ ) **do**
- Repeat lines 6–10
- 15: end for
- 16: **return** Optimized  $\hat{\sigma}_t^*$

noise behavior, yet in practice, noise interacts with image structure in resolution-sensitive ways. While modern diffusion models can generate images at arbitrary resolutions, our analysis shows that quality degradation at unseen resolutions may stem from this overlooked resolution-dependent misalignment.

### 3.3. Resolution-Aware Test-Time Calibration

While recent methods have extended diffusion models to arbitrary resolutions by adapting token lengths or position encodings [28], we focus instead on correcting forward-reverse misalignment through test-time adjustment of the conditioning noise level. Rather than modifying the sampling trajectory or retraining the model, we propose a lightweight post-processing procedure that adjusts only the input noise level  $\hat{\sigma}_t$  passed to the denoiser at each timestep.

Role of Noise-Level Embedding. At each timestep, diffusion models receive not only the noisy latent  $\mathbf{x}_t$  but also a noise-level or timestep embedding that encodes the expected magnitude of corruption in the input. This embedding allows the model to adapt its prediction of the denoised image based on how noisy the input is: for low noise, the model performs minor corrections, whereas for high noise, it applies stronger denoising. In our framework, the conditioning noise  $\hat{\sigma}_t$  is directly mapped to this embedding. Consequently, by manipulating  $\hat{\sigma}_t$  at test time, we can explicitly interfere how the model interprets the noise level in the input, enabling a resolution-aware correction without changing the learned weights or the sampling schedule.

**Problem Setup.** Let  $\phi$  denote a trained flow-matching diffusion model with a predefined noise schedule  $\sigma_t t = 0^T$ . At each timestep t, the model receives a noisy latent  $\mathbf{x}_{t+1}$  and a noise-level embedding derived from a conditioning noise  $\hat{\sigma}_t$ . This embedding informs the network how much noise to expect and guides its prediction of the velocity field  $\phi(\mathbf{x}_{t+1}, \hat{\sigma}_t)$ .

In standard sampling,  $\hat{\sigma}_t = \sigma_t$  follows the original noise schedule. In our approach, we allow  $\hat{\sigma}_t$  to differ from  $\sigma_t$  to correct forward–reverse misalignment at test time. By tuning  $\hat{\sigma}_t$ , we can adapt the model's denoising behavior to different resolutions without changing the learned weights or sampling procedure.

Given a noisy latent input  $\mathbf{x}_{t+1}$ , we expect  $\mathbf{x}_t$  to match the forward sample obtained by applying Gaussian noise to a clean latent  $\mathbf{x}_0$ . Our goal is to find a conditioning noise level  $\hat{\sigma}_t$  such that the denoised prediction  $\hat{\mathbf{x}}_t$  minimizes the discrepancy from  $\mathbf{x}_t$ :

$$\hat{\mathbf{x}}_{t} = \mathbf{x}_{t+1} + \phi(\mathbf{x}_{t+1}, \hat{\sigma}_{t}) \cdot \Delta t, \quad \text{where } \Delta t = \sigma_{t+1} - \sigma_{t},$$

$$\hat{\sigma}_{t}^{*} = \arg\min_{\hat{\sigma}} \|\hat{\mathbf{x}}_{t} - \mathbf{x}_{t}\|^{2}.$$
(5)

Coarse-to-Fine Search Strategy. We estimate  $\hat{\sigma}_t^*$  via a coarse-to-fine grid search that minimizes the one-step reverse error at each timestep. Starting from the final step t=T-1, we proceed backward in time. For each t, we first evaluate the default conditioning  $\hat{\sigma}_t = \sigma_t$ , then perform a coarse

Algorithm 2 Euler Sampling with Calibrated Conditioning

```
Require: Model \phi, initial latent \mathbf{x}_T, noise schedule \{\sigma_t\}_{t=0}^T, calibrated conditioning \{\hat{\sigma}_t^*\}_{t=0}^{T-1}

1: for t = T - 1 to 0 do

2: \mathbf{v}_t \leftarrow \phi(\mathbf{x}_{t+1}, \hat{\sigma}_t^*)

3: \mathbf{x}_t \leftarrow \mathbf{x}_{t+1} + \mathbf{v}_t \cdot (\sigma_{t+1} - \sigma_t)

4: end for

5: return \mathbf{x}_0
```

sweep with a larger stride  $\delta_c$  to identify a promising region. A subsequent fine-grained search with a smaller stride  $\delta_f$  refines the estimate within a narrow window.

To ensure monotonic consistency with the diffusion trajectory, we constrain all candidate values to lie in  $[0, \hat{\sigma}^*_{t+1}]$ . This backward recursion allows us to progressively calibrate the denoising inputs while respecting the ordering of noise levels. The full procedure is detailed in Algorithm 1.

We perform this calibration over a small set of image-text pairs for each resolution. The resulting schedule  $\{\hat{\sigma}_t^*\}$  is resolution-specific and cached for reuse at inference.

Inference with Calibrated Conditioning. At inference time, we sample using the original noise schedule  $\{\sigma_t\}$  to preserve the intended diffusion trajectory. However, at each timestep t, we replace the model input conditioning with the precomputed value  $\hat{\sigma}_t^*$  obtained from the calibration procedure. These values are resolution-specific but fixed across inputs, and require no model retraining or architectural changes. As shown in Algorithm 2, the update step becomes:

$$\mathbf{x}_t = \mathbf{x}_{t+1} + \phi(\mathbf{x}_{t+1}, \hat{\sigma}_t^*) \cdot (\sigma_{t+1} - \sigma_t). \tag{6}$$

### 4. Experimental Setup

Implementation Details. For small-scale lightweight calibration, we randomly sample 200 web-crawled images from SBU [27]. These samples are only used to estimate resolution-specific conditioning noise levels. For all experiments, we use a coarse-to-fine search strategy with a coarse search window  $\epsilon_c=0.1$  and a fine search window  $\epsilon_f=0.01$ . Experiments are conducted on NVIDIA A40s. On a single A40 GPU, calibrating on a 128×128 image takes around 30 seconds for SD3, 70 seconds for SD3.5, and 100 seconds for Flux-Dev.

**Datasets.** We evaluate on LAION-COCO [35], a diverse subset of LAION-5B [34] containing multi-resolution images with BLIP-generated captions [20]. It includes a broad spectrum of content, such as objects, people, and natural scenes. We also include an evaluation on the CelebA benchmark [24], a face-centric image—text dataset.

Table 1. Quantitative evaluation on CelebA across resolutions. We report CLIP score ( $\uparrow$ ) and FID ( $\downarrow$ ) for SD3 and SD3.5 with and without our calibration. Superscript percentages show relative improvements (violet) or degradations (gray).

|           |       | SD3                             |                                   | SD3.5                           |                                   |
|-----------|-------|---------------------------------|-----------------------------------|---------------------------------|-----------------------------------|
|           |       | CLIP↑                           | FID↓                              | CLIP↑                           | FID↓                              |
| 128×128   | Base  | 21.07                           | 320.45                            | 19.01                           | 386.86                            |
|           | +Ours | <b>21.86</b> <sup>+3.75</sup> % | <b>311.89</b> <sup>+2.67</sup> %  | <b>20.56</b> <sup>+8.15</sup> % | 374.74 <sup>+3.13%</sup>          |
| 256×256   | Base  | 22.14                           | 291.26                            | 19.96                           | 359.00                            |
|           | +Ours | 23.76 <sup>+7.32</sup> %        | <b>252.61</b> <sup>+13.27</sup> % | <b>20.21</b> <sup>+1.25%</sup>  | <b>271.52</b> <sup>+24.37</sup> % |
| 512×512   | Base  | 25.54                           | 128.62                            | 22.27                           | 292.42                            |
|           | +Ours | <b>25.74</b> <sup>+0.78</sup> % | <b>123.14</b> <sup>+4.26</sup> %  | 23.51 <sup>+5.57</sup> %        | <b>270.36</b> <sup>+7.54</sup> %  |
| 768×768   | Base  | 27.02                           | 93.66                             | 26.68                           | 135.84                            |
|           | +Ours | <b>27.03</b> <sup>+0.04</sup> % | <b>93.14</b> <sup>+0.56%</sup>    | <b>26.91</b> <sup>+0.86</sup> % | <b>127.17</b> <sup>+6.38</sup> %  |
| 1024×1024 | Base  | 25.07                           | 132.65                            | 26.66                           | 96.27                             |
|           | +Ours | <b>25.08</b> <sup>+0.04</sup> % | <b>131.99</b> <sup>+0.50%</sup>   | 26.66 <sup>+0.00%</sup>         | <b>96.10</b> <sup>+0.18%</sup>    |

**Metrics.** We evaluate models with standard text-to-image generation metrics: CLIP Score [14] for text-image alignment and Frechet Inception Distance (FID) [15] for the distance between feature distributions of real and generated images.

**Models.** We validate our method on flow-matching diffusion models with various configurations. We integrate it to Stable Diffusion 3 [8] with a linear noise schedule and Stable Diffusion 3.5 [8] with a non-linear schedule that spends more time in low- or high-noise regimes. We also experiment with Flux-Dev [6], an open-sourced distilled flow-matching DiT model that incorporates a resolution-aware scheduler that applies a shift parameter based on image size.

### 5. Experimental Results

### 5.1. Fixed Linear or Non-linear Noise Schedules

We evaluate NoiseShift using two flow-matching diffusion models with fixed noise schedules (See Figure 2). Stable Diffusion 3 (SD3) uses a linear noise schedule shared across resolutions, while Stable Diffusion 3.5 (SD3.5) adopts a fixed non-linear schedule that biases sampling toward low-or high-noise regimes.

We conduct inference with calibrated noise schedulers across resolutions with SD3 and SD3.5. As shown in Table 1, NoiseShift consistently improves CLIP Score and FID for both SD3 and SD3.5 across non-default resolutions ranging from 128×128 to 768×768. At the default resolution of 1024×1024, performance remains unchanged, confirming that NoiseShift preserves the fidelity when no calibration is needed. Similar trends hold on LAION-COCO (Table 2), where resolution-aware conditioning improves the generation quality without fine-tuning the underlying model.

These results demonstrate that NoiseShift effectively mitigates forward–reverse mismatch at lower resolutions. Since

Table 2. Quantitative evaluation on LAION-COCO across resolutions. We report CLIP score ( $\uparrow$ ) and FID ( $\downarrow$ ) for SD3 and SD3.5 with and without our calibration. Superscript percentages show relative improvements (violet) or degradations (gray).

|           |       | S                               | SD3                              |                                 | SD3.5                             |  |
|-----------|-------|---------------------------------|----------------------------------|---------------------------------|-----------------------------------|--|
|           |       | CLIP↑                           | FID↓                             | CLIP↑                           | FID↓                              |  |
| 128×128   | Base  | 19.80                           | 203.23                           | 19.18                           | 310.40                            |  |
|           | +Ours | <b>21.07</b> <sup>+6.41</sup> % | <b>170.93</b> <sup>+15.89%</sup> | <b>19.75</b> <sup>+2.97</sup> % | <b>276.90</b> <sup>+10.79</sup> % |  |
| 256×256   | Base  | 22.24                           | 159.13                           | 19.46                           | 256.31                            |  |
|           | +Ours | 23.28 <sup>+4.68</sup> %        | <b>130.84</b> <sup>+17.78%</sup> | <b>20.23</b> <sup>+3.96%</sup>  | <b>175.14</b> <sup>+31.67</sup> % |  |
| 512×512   | Base  | 28.52                           | 76.49                            | 22.26                           | 203.55                            |  |
|           | +Ours | <b>28.61</b> <sup>+0.32%</sup>  | <b>75.86</b> <sup>+0.82%</sup>   | <b>23.41</b> <sup>+5.17%</sup>  | <b>174.20</b> <sup>+14.42%</sup>  |  |
| 768×768   | Base  | 30.10                           | 55.13                            | 31.15                           | 45.05                             |  |
|           | +Ours | 30.10 <sup>+0.00%</sup>         | 55.07 <sup>+0.11%</sup>          | <b>31.28</b> <sup>+0.42</sup> % | <b>42.05</b> <sup>+6.66%</sup>    |  |
| 1024×1024 | Base  | 29.26                           | 94.53                            | 31.62                           | 47.65                             |  |
|           | +Ours | <b>29.22</b> <sup>-0.14</sup> % | <b>95.24</b> <sup>-0.75%</sup>   | 31.62 <sup>+0.00%</sup>         | <b>47.69</b> <sup>-0.08</sup> %   |  |

it does not modify the model architecture or training objective, it is naturally upper-bounded by the model's original generative capability. Nonetheless, it provides measurable quality gains through simple post-hoc calibration when applied to lower resolutions.

### **5.2.** Calibrated Noise Conditioning

Figure 4 visualizes the calibrated conditioning noise levels  $\hat{\sigma}_t$  from our method across resolutions for SD3 (left) and SD3.5 (right). At the default resolution of  $1024 \times 1024$ , the calibrated curves closely match the original schedule, confirming that the forward–reverse alignment is intact at the training resolution. In contrast, for lower resolutions, optimal  $\hat{\sigma}_t$  trajectories consistently shift above the default schedule, indicating that higher conditioning noise levels are needed to correct resolution-specific misalignment.

This behavior supports our core hypothesis: the same sampling noise level  $\sigma_t$  has resolution-dependent perceptual effects, which can be effectively mitigated by adjusting only the conditioning noise level during inference. Notably, the magnitude of deviation from the default schedule increases as resolution decreases, aligning with the observed degradation in visual quality (see Figure 1). This trend holds across both SD3 and SD3.5 despite their differing noise schedule shapes.

### **5.3.** Time Shifting Noise Scheduler

We further evaluate NoiseShift on Flux-Dev [6], a distilled flow-matching DiT model that incorporates a resolution-aware time-shift parameter. The noise schedule in Flux-Dev shifts depending on the target resolution: higher-resolution images retain larger  $\sigma_t$  values for longer, effectively extending their time in high-signal regimes.

While Flux-Dev adjusts the actual sampling schedule based on resolution, NoiseShift instead calibrates the *conditioning input* to the denoiser without altering the forward



Figure 3. **Qualitative comparison of Flux-Dev.** Generated image examples before and after applying NoiseShift are on CelebA (left) and LAION-COCO (right).

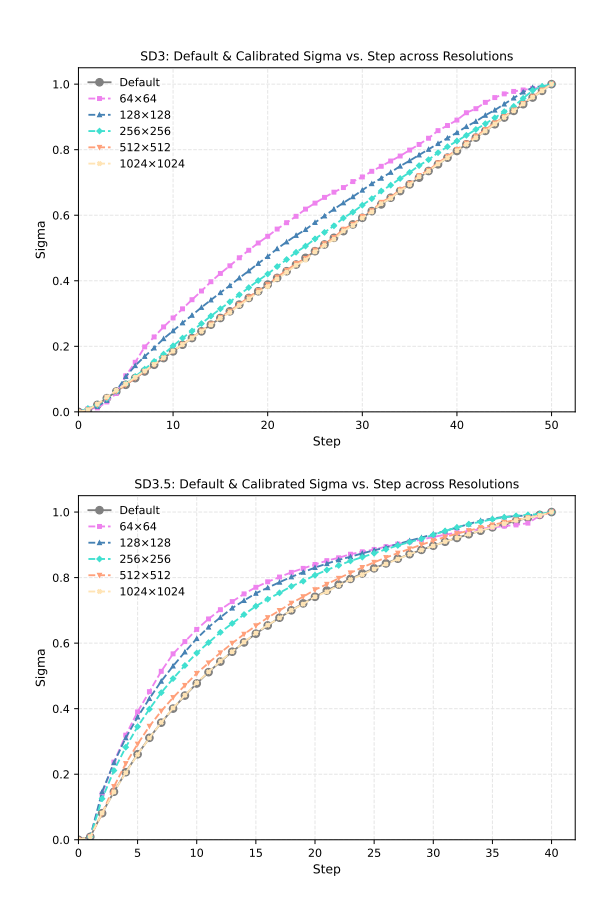


Figure 4. Calibrated conditioning noise levels across resolutions. We plot the default sampling noise schedule (gray) alongside the resolution-specific calibrated conditioning  $\hat{\sigma}_t$  for SD3 (left) and SD3.5 (right). At the default resolution (1024×1024), the curves align closely. At lower resolutions, the optimal  $\hat{\sigma}_t$  curves consistently deviate upward, reflecting a need for stronger conditioning to compensate for perceptual degradation.

noise schedule itself. In that sense, our approach operates as a lightweight test-time correction, "cheating" the model's

Table 3. Quantitative evaluation of Flux-Dev across resolutions. We report CLIP score ( $\uparrow$ ) and FID ( $\downarrow$ ) on LAION-COCO and CelebA with and without our calibration. Superscript percentages show relative improvements (violet) or degradations (gray).

|           |               | LAION-COCO                       |                                 | CelebA                                   |                                       |
|-----------|---------------|----------------------------------|---------------------------------|--|---------------------------------------|
|           |               | CLIP↑                            | FID↓                            | CLIP↑                                    | FID↓                                  |
| 64×64     | Base<br>+Ours |                                  | $119.60 \\ 113.32^{+4.80\%}$    | 27.70<br><b>27.77</b> <sup>+0.25</sup> % | $182.96 \\ \textbf{177.03}^{+4.22\%}$ |
| 128×128   | Base          | 30.74                            | 48.00                           | 28.75                                    | 90.62                                 |
|           | +Ours         | <b>30.83</b> <sup>+0.29</sup> %  | <b>47.45</b> <sup>+1.15</sup> % | <b>28.64</b> <sup>-0.38%</sup>           | <b>87.63</b> <sup>+3.30%</sup>        |
| 256×256   | Base          | 32.30                            | 26.72                           | 27.89                                    | 56.33                                 |
|           | +Ours         | 32.33 <sup>+0.09%</sup>          | 25.82 <sup>+3.37</sup> %        | 27.89 <sup>+0.00%</sup>                  | 55.52 <sup>+1.44%</sup>               |
| 512×512   | Base          | 32.55                            | 20.13                           | 28.44                                    | 87.86                                 |
|           | +Ours         | 32.55 <sup>+0.00</sup> %         | <b>19.62</b> <sup>+2.53</sup> % | <b>28.45</b> <sup>+0.04%</sup>           | <b>86.45</b> <sup>+1.60%</sup>        |
| 768×768   | Base          | 32.58                            | 19.10                           | 27.90                                    | 75.52                                 |
|           | +Ours         | <b>32.60</b> <sup>+0.06</sup> %  | 19.03 <sup>+0.37</sup> %        | <b>28.10</b> <sup>+0.72%</sup>           | <b>72.10</b> <sup>+4.53%</sup>        |
| 1024×1024 | Base<br>+Ours | 32.82<br>32.80 <sup>-0.06%</sup> |                                 | 27.92<br><b>28.12</b> <sup>+0.72</sup> % |                                       |

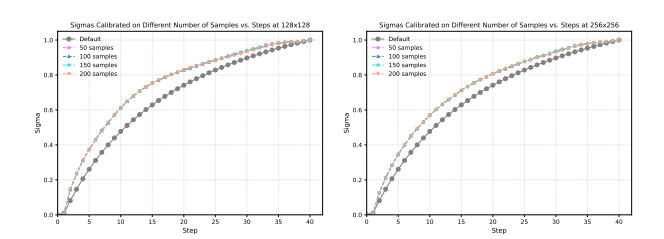


Figure 5. **Ablation studies.** Ablation studies on the number of samples used during calibration and the new sigmas obtained at  $128 \times 128$  and  $256 \times 256$ .

expectations without modifying its architecture or training.

As shown in Table 3, NoiseShift provides consistent improvements from  $64 \times 64$  to  $768 \times 768$  on LAION-COCO and CelebA. Although gains are modest, they are notable given that Flux-Dev is a distilled model and our method requires no finetunning. Interestingly, at  $1024 \times 1024$ , performance



Figure 6. **Qualitative comparison of SD3.5**. Generated image examples before and after applying NoiseShift are on CelebA (top) and LAION-COCO (bottom).

remains unchanged or slightly reduced, likely because it is the resolution of the final stage training, reducing the impact of calibration. These results suggest that NoiseShift complements, but does not replace, the resolution-aware scheduling baked into the model itself.

### 5.4. Ablation Studies

This section studies the number of samples used in the Noise-Shift calibration. As shown in Figure 5, even though the number of samples varies from 50 to 200, the calibrated sigmas always converge in almost the same range. Given the fact that the calibration already has a very low computation cost, reducing the number of samples can lead to an almost free re-calibration, which improves the low-resolution image generation quality.

### 5.5. Qualitative Results

In Figure 7 and Figure 6, we present qualitative examples of SD3 and SD3.5 [9] before and after applying NoiseShift on CelebA and LAION-COCO. Across all resolutions, NoiseShift improves the overall image quality, providing better structure and textures of the generated images. In Figure 3, we show how NoiseShift improves the Flux-Dev model down to  $64 \times 64$  resolutions. Overall, we observe the quality improvement and fewer artifacts across the resolutions.

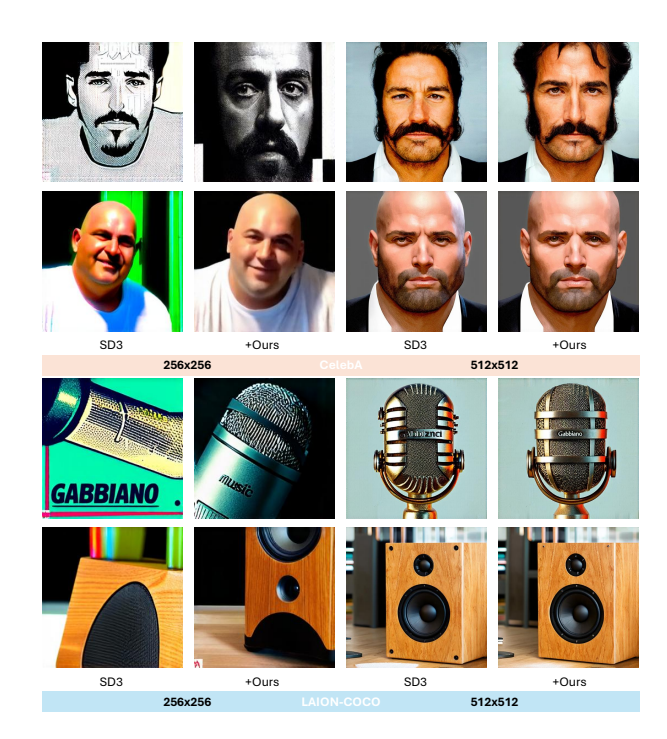


Figure 7. **Qualitative comparison of SD3.5**. Generated image examples before and after applying NoiseShift are on CelebA (top) and LAION-COCO (bottom).

### 6. Conclusion

We identify resolution-dependent exposure bias as a key contributor to quality degradation in state-of-the-art diffusion models when sampling at lower resolutions. To address this, we introduced NoiseShift, a simple, training-free approach that recalibrates the denoising conditioning to better align with resolution-specific noise distributions. Our method consistently improves image quality across resolutions and is complementary to both noise schedule modifications and architectural enhancements, making it readily applicable to recent advances in text-to-image generation.

Limitations and Future Work. While NoiseShift mitigates exposure bias and enhances cross-resolution performance, it does not fully solve the challenge of low-resolution generalization. Future work may explore integrating NoiseShift with learned adapters, dynamic token routing, or resolution-specific fine-tuning strategies.

**Broader Impact.** By enhancing sample quality at low resolutions, NoiseShift increases the adaptability of text-to-image systems to diverse deployment settings, including mobile and assistive applications. However, the ability to generate increasingly high-quality synthetic content may also exacerbate issues around misinformation and image provenance, highlighting the need for responsible use and effective detection mechanisms.

### References

- [1] Stability AI. Stable diffusion 3. https://stability.ai/news/stable-diffusion-3-announcement, 2024.3
- [2] Omer Bar-Tal, Lior Yariv, Yaron Lipman, and Tali Dekel. Multidiffusion: Fusing diffusion paths for controlled image generation. In *ICML*, 2023. 1, 2
- [3] Ting Chen. On the importance of noise scheduling for diffusion models. *arXiv*, 2023. 3
- [4] Ting Chen. On the importance of noise scheduling for diffusion models. *arXiv* preprint arXiv:2301.10972, 2023. 2
- [5] Jiaxiang Cheng, Pan Xie, Xin Xia, Jiashi Li, Jie Wu, Yuxi Ren, Huixia Li, Xuefeng Xiao, Min Zheng, and Lean Fu. Resadapter: Domain consistent resolution adapter for diffusion models. ArXiv, abs/2403.02084, 2024. 1, 2
- [6] Cody Crockett, Tushar Patil, Laura Weidinger, et al. Flux: A modern diffusion transformer. https://github.com/ fluxml/flux-diffusion, 2024. 1, 2, 3, 6
- [7] Ruoyi Du, Dongliang Chang, Timothy Hospedales, Yi-Zhe Song, and Zhanyu Ma. Demofusion: Democratising highresolution image generation with no \$\$\$. In Proceedings of the IEEE/CVF Conference on Computer Vision and Pattern Recognition, pages 6159–6168, 2024. 1, 2
- [8] Patrick Esser, Sumith Kulal, A. Blattmann, Rahim Entezari, Jonas Muller, Harry Saini, Yam Levi, Dominik Lorenz, Axel Sauer, Frederic Boesel, Dustin Podell, Tim Dockhorn, Zion English, Kyle Lacey, Alex Goodwin, Yannik Marek, and Robin Rombach. Scaling rectified flow transformers for highresolution image synthesis. ArXiv, abs/2403.03206, 2024.
- [9] Patrick Esser, Sumith Kulal, Andreas Blattmann, Rahim Entezari, Jonas Müller, Harry Saini, Yam Levi, Dominik Lorenz, Axel Sauer, Frederic Boesel, et al. Scaling rectified flow transformers for high-resolution image synthesis. In Forty-first international conference on machine learning, 2024. 1, 2, 8
- [10] Lanqing Guo, Yingqing He, Haoxin Chen, Menghan Xia, Xiaodong Cun, Yufei Wang, Siyu Huang, Yong Zhang, Xintao Wang, Qifeng Chen, et al. Make a cheap scaling: A self-cascade diffusion model for higher-resolution adaptation. In European Conference on Computer Vision, pages 39–55. Springer, 2024. 2
- [11] Qiushan Guo, Sifei Liu, Yizhou Yu, and Ping Luo. Rethinking the noise schedule of diffusion-based generative models. 2023.
- [12] Moayed Haji-Ali, Guha Balakrishnan, and Vicente Ordonez. Elastic diffusion: Training-free arbitrary size image generation through global-local content separation, 2024. 1, 2, 3
- [13] Yingqing He, Shaoshu Yang, Haoxin Chen, Xiaodong Cun, Menghan Xia, Yong Zhang, Xintao Wang, Ran He, Qifeng Chen, and Ying Shan. Scalecrafter: Tuning-free higherresolution visual generation with diffusion models. In *The Twelfth International Conference on Learning Representa*tions, 2023. 2, 3
- [14] Jack Hessel, Ari Holtzman, Maxwell Forbes, Ronan Le Bras, and Yejin Choi. Clipscore: A reference-free evaluation metric for image captioning. ArXiv, abs/2104.08718, 2021. 6

- [15] Martin Heusel, Hubert Ramsauer, Thomas Unterthiner, Bernhard Nessler, and Sepp Hochreiter. Gans trained by a two time-scale update rule converge to a local nash equilibrium. In Neural Information Processing Systems, 2017. 6
- [16] Emiel Hoogeboom, Jonathan Heek, and Tim Salimans. Simple diffusion: End-to-end diffusion for high resolution images. In *Proceedings of the 40th International Conference on Machine Learning (ICML)*, 2023. 1, 2
- [17] Linjiang Huang, Rongyao Fang, Aiping Zhang, Guanglu Song, Si Liu, Yu Liu, and Hongsheng Li. Fouriscale: A frequency perspective on training-free high-resolution image synthesis. In *European Conference on Computer Vision*, pages 196–212. Springer, 2024. 1
- [18] Juno Hwang, Yong-Hyun Park, and Junghyo Jo. Resolution chromatography of diffusion models. arXiv preprint arXiv:2401.10247, 2023.
- [19] Zhiyu Jin, Xuli Shen, Bin Li, and Xiangyang Xue. Training-free diffusion model adaptation for variable-sized text-to-image synthesis. Advances in Neural Information Processing Systems, 36:70847–70860, 2023. 3
- [20] Junnan Li, Dongxu Li, Caiming Xiong, and Steven C. H. Hoi. Blip: Bootstrapping language-image pre-training for unified vision-language understanding and generation. In *International Conference on Machine Learning*, 2022. 5
- [21] Mingxiao Li, Tingyu Qu, Ruicong Yao, Wei Sun, and Marie-Francine Moens. Alleviating exposure bias in diffusion models through sampling with shifted time steps. *arXiv* preprint *arXiv*:2305.15583, 2023. 1, 3
- [22] Yotam Lipman, Emiel Hoogeboom, Ajay Jain, Jacob Menick, Arash Vahdat, Tim Salimans, David J Fleet, and Jonathan Heek. Flow matching for generative modeling. arXiv preprint arXiv:2305.08891, 2023. 3
- [23] Hanyu Liu, Zhen Xu, Wei Shi, Yuntao Bai, Hongyuan Zhao, Stefano Ermon, and Xiao Wang. Flow matching models for learning reliable dynamics. *arXiv preprint arXiv:2305.19591*, 2023. 3
- [24] Ziwei Liu, Ping Luo, Xiaogang Wang, and Xiaoou Tang. Deep learning face attributes in the wild. In *Proceedings of International Conference on Computer Vision (ICCV)*, 2015.
- [25] Cheng Lu, Yuhao Zhou, Fan Bao, Jianfei Chen, Chongxuan Li, and Jun Zhu. Dpm-solver: A fast ode solver for diffusion probabilistic model sampling in around 10 steps. Advances in Neural Information Processing Systems, 35:5775–5787, 2022.
- [26] Cheng Lu, Yuhao Zhou, Fan Bao, Jianfei Chen, Chongxuan Li, and Jun Zhu. Dpm-solver++: Fast solver for guided sampling of diffusion probabilistic models. arXiv preprint arXiv:2211.01095, 2022. 3
- [27] Vicente Ordonez, Girish Kulkarni, and Tamara L. Berg. Im2text: Describing images using 1 million captioned photographs. In *Neural Information Processing Systems*, 2011.
- [28] William Peebles and Saining Xie. Scalable Diffusion Models with Transformers. In *Proceedings of the IEEE/CVF International Conference on Computer Vision (ICCV)*, pages 4195–4205, 2023. 1, 5

- [29] Dustin Podell, Zion English, Kyle Lacey, Andreas Blattmann, Tim Dockhorn, Jonas Müller, Joe Penna, and Robin Rombach. Sdxl: Improving latent diffusion models for high-resolution image synthesis. arXiv, 2023. 1
- [30] Dustin Podell, Zion English, Kyle Lacey, Andreas Blattmann, Tim Dockhorn, Jonas Müller, Joe Penna, and Robin Rombach. Sdxl: Improving latent diffusion models for high-resolution image synthesis. arXiv preprint arXiv:2307.01952, 2023. 1
- [31] Haonan Qiu, Shiwei Zhang, Yujie Wei, Ruihang Chu, Hangjie Yuan, Xiang Wang, Yingya Zhang, and Ziwei Liu. Freescale: Unleashing the resolution of diffusion models via tuning-free scale fusion. *arXiv* preprint arXiv:2412.09626, 2024. 1, 2
- [32] Robin Rombach, Andreas Blattmann, Dominik Lorenz, Patrick Esser, and Björn Ommer. High-resolution image synthesis with latent diffusion models. In *Proceedings of the IEEE/CVF conference on computer vision and pattern recognition*, pages 10684–10695, 2022. 1
- [33] Olaf Ronneberger, Philipp Fischer, and Thomas Brox. U-net: Convolutional networks for biomedical image segmentation. In *Medical image computing and computer-assisted interven*tion, 2015. 1
- [34] Christoph Schuhmann, Romain Beaumont, Richard Vencu, Cade Gordon, Ross Wightman, Mehdi Cherti, Theo Coombes, Aarush Katta, Clayton Mullis, Mitchell Wortsman, Patrick Schramowski, Srivatsa Kundurthy, Katherine Crowson, Ludwig Schmidt, Robert Kaczmarczyk, and Jenia Jitsev. Laion-5b: An open large-scale dataset for training next generation image-text models. ArXiv, abs/2210.08402, 2022. 5
- [35] Christoph Schuhmann, Andreas A. K" opf, Theo Coombes Richard Vencu, and Ross Beaumont. Laioncoco: 600m synthetic captions from laion2b-en, 2023. 5
- [36] Sitian Shen, Zilin Zhu, Linqian Fan, Harry Zhang, and Xinxiao Wu. Diffclip: Leveraging stable diffusion for language grounded 3d classification. In *Proceedings of the IEEE/CVF Winter Conference on Applications of Computer Vision*, pages 3596–3605, 2024. 1
- [37] Shitao Xiao, Yueze Wang, Junjie Zhou, Huaying Yuan, Xingrun Xing, Ruiran Yan, Chaofan Li, Shuting Wang, Tiejun Huang, and Zheng Liu. Omnigen: Unified image generation. arXiv preprint arXiv:2409.11340, 2024.
- [38] Lvmin Zhang, Anyi Rao, and Maneesh Agrawala. Adding conditional control to text-to-image diffusion models. In *Proceedings of the IEEE/CVF international conference on computer vision*, pages 3836–3847, 2023. 1
- [39] Yiming Zhang, Yicheng Gu, Yanhong Zeng, Zhening Xing, Yuancheng Wang, Zhizheng Wu, and Kai Chen. Foleycrafter: Bring silent videos to life with lifelike and synchronized sounds. *arXiv preprint arXiv:2407.01494*, 2024. 1, 2
- [40] Qingping Zheng, Yuanfan Guo, Jiankang Deng, Jianhua Han, Ying Li, Songcen Xu, and Hang Xu. Any-size-diffusion: Toward efficient text-driven synthesis for any-size hd images. In *Proceedings of the AAAI Conference on Artificial Intelligence*, pages 7571–7578, 2024. 1, 2
- [41] Zhen Zou, Hu Yu, Jie Xiao, and Feng Zhao. Exposure bias reduction for enhancing diffusion transformer feature caching. *arXiv preprint arXiv:2503.07120*, 2025. 1